

A survey of SiO 5→4 emission towards outflows from massive young stellar objects

A.G. Gibb¹, C.J. Davis², T.J.T. Moore³

¹ Department of Physics and Astronomy, University of British Columbia, 6224 Agricultural Road, Vancouver, BC, V6T 1Z1, Canada

² Joint Astronomy Centre, 660 N. A'ohoku Place, University Park, Hilo, HI 96720, USA

³ Astrophysics Research Institute, Liverpool John Moores University, Twelve Quays House, Egerton Wharf, Birkenhead, CH41 1LD

Accepted 2007 September 10. Received 2007 August 22; in original form 2007 April 19

ABSTRACT

Results are presented of a survey of SiO 5→4 emission observed with the James Clerk Maxwell Telescope (JCMT) towards a sample of outflows from massive young stellar objects. The sample is drawn from a single-distance study by Ridge & Moore and allows the reasons that govern the detectability of SiO to be explored without the bias introduced by observing sources at different distances. This is the first such unbiased survey of SiO emission from massive outflows. In a sample of 12 sources, the 5→4 line was detected in 5, a detection rate of 42 per cent. This detection rate is higher than that found for a sample of low-luminosity outflow sources, although for sources of comparable luminosity, it is in good agreement with the results of a previous survey of high luminosity sources. For most of the detected sources, the 5→4 emission is compact or slightly extended along the direction of the outflow. NGC 6334I shows a clear bipolar flow in the 5→4 line. Additional data were obtained for W3-IRS5, AFGL 5142 and W75N for the 2→1 transition of SiO using the Berkeley-Illinois-Maryland Association (BIMA) millimetre interferometer. There is broad agreement between the appearance of the SiO emission in both lines, though there are some minor differences. The 2→1 emission in AFGL 5142 is resolved into two outflow lobes which are spatially coincident on the sky, in good agreement with previous observations. In general the SiO emission is clearly associated with the outflow. Simple analysis and radiative transfer modelling of the detected sources yield similar SiO column densities. The abundance of SiO is $\sim 0.1\text{--}7.0 \times 10^{-9}$, and the H₂ number density is within a factor of two of 10^5 cm^{-3} . However, the temperature is not constrained over the range 50–150 K. The primary indicator of SiO 5→4 detectability is the outflow velocity, i.e. the presence of SiO is an indicator of a high velocity outflow. This result is consistent with the existence of a critical shock velocity required to disrupt dust grains and subsequent SiO formation in post-shock gas. There is also weak evidence that higher luminosity sources and denser outflows are more likely to be detected.

Key words: stars: formation – ISM: abundances – ISM: jets and outflows – ISM: molecules – radio lines: ISM

1 INTRODUCTION

Silicon monoxide (SiO) is formed when strong shocks passing through dense molecular gas disrupt dust grains (e.g. Caselli, Hartquist, & Havnes 1997, Schilke et al. 1997). The gas-phase abundance of SiO is observed to be negligible in quiescent regions (e.g. Irvine, Goldsmith & Hjalmarsen 1987; Ziurys, Friberg & Irvine 1989), but can be many orders of magnitude higher in molecular outflows (e.g. Martín-Pintado, Bachiller & Fuente 1992). Gibb et al. (2004, hereafter Paper I) observed the $J=5\rightarrow 4$ transition towards a sample of 25 low-mass outflows with a detection rate of ~ 28 per cent. Their results showed that SiO emission was preferentially detected towards the youngest – class 0 – sources. They concluded that the combination of greater mean density in class 0 environments coupled with a high outflow velocity favoured the

production and excitation of the $J=5\rightarrow 4$ transition of SiO to a detectable level.

However, one criticism that can be made of the survey in Paper I is that the sample contained sources at different distances, and thus it is possible that the non-detections of more distant sources was due to the non-uniform sensitivity. This also means that correlations (or the lack thereof) between source parameters may be biased. In order to overcome this limitation, a followup survey has been carried out in the same transition but this time of outflows from high-mass young stellar objects (YSOs) all of which are located at the same distance of ~ 2.0 kpc. The sample is composed of 10 of the 11 sources from the CO survey of Ridge & Moore (2001, hereafter RM01) with two additional sources at the same distance with well-studied outflows. The primary reason for uti-

Table 1. Sample summary. The columns are: Source name, IRAS identification, Galactic position, J2000 right ascension and declination, distance, LSR velocity, bolometric luminosity and mass of the core in which the YSO is embedded. The notation $a(b)$ is shorthand for $a \times 10^b$. Note that W75N has no counterpart in the IRAS point source catalogue. Distances, LSR velocities and luminosities are from RM01, Gibb et al. (2003) and Shepherd et al. (1998). Masses are obtained from the literature (sources described in the text).

| Source | IRAS identification | l, b (deg) | RA (J2000) | Dec (J2000) | d (kpc) | v_{LSR} (km s^{-1}) | L_{bol} (L_{\odot}) | M (M_{\odot}) |
|-----------------|---------------------|-----------------|--|----------------|--------------|--|-------------------------------------|------------------------|
| Detections | | | | | | | | |
| W3-IRS5 | 02219+6152 | 133.71+1.21 | 02 ^h 25 ^m 38 ^s .6 | 62°05′52″.2 | 2.3 | −40 | 1.1(6) | 800 |
| AFGL 5142 | 05264+3345 | 174.20−0.07 | 05 30 48.0 | 33 47 53.5 | 1.8 | −4 | 3.8(3) | 145 |
| NGC6334I | 17175−3544 | 351.42+0.64 | 17 20 53.2 | −35 46 59.5 | 1.7 | −5 | 8.0(4) | 200 |
| G35.2−0.7N | 18556+0136 | 35.19−0.74 | 18 58 12.9 | 01 40 36.5 | 2.0 | +34 | 2.0(4) | 800 |
| W75N | — | 81.87+0.78 | 20 38 36.4 | 42 37 37.5 | 2.0 | +8 | 1.4(5) | ~350 |
| Non-detections | | | | | | | | |
| AFGL 437 | 03035+5819 | 139.91+0.20 | 03 07 24.7 | 58 30 55.3 | 2.0 | −39 | 2.4(4) | <1500 |
| AFGL 5157 | 05345+3157 | 176.51+0.20 | 05 37 50.9 | 32 00 03.8 | 1.8 | −19 | 5.5(3) | 179 |
| G192.16−3.82 | 05553+1631 | 192.16−3.82 | 05 58 13.6 | 16 31 58.3 | 2.0 | +6 | 3.3(3) | 100 |
| GGD27-IRS1 | 18162−2048 | 10.84−2.59 | 18 19 12.6 | −20 47 31.6 | 1.7 | +12 | 2.0(4) | 200 |
| S88B | 19446+2505 | 61.48+0.09 | 19 46 48.5 | 25 12 56.2 | 2.0 | +20 | 1.8(5) | 450 |
| IRAS 19550+3248 | 19550+3248 | 69.25+2.14 | 19 56 55.0 | 32 56 34.7 | 2.0 | +12 | 1.5(2) | 220 |
| IRAS 20188+3928 | 20188+3928 | 77.46+1.76 | 20 20 38.1 | 39 38 06.8 | 2.0 | +2 | 1.3(4) | 800 |

Table 2. Details of sensitivity and detections for the SiO 5→4 observations. The values for the non-detections are 3- σ upper limits.

| Source | Peak T_{MB} (K) | σ (K) | $\int T_{\text{MB}} dv$ (K km s^{-1}) | σ (K km s^{-1}) |
|-----------------|-----------------------------|-----------------|---|--------------------------------------|
| Detections | | | | |
| W3-IRS5 | 0.37 | 0.04 | 2.38 | 0.33 |
| AFGL 5142 | 0.92 | 0.05 | 7.73 | 0.45 |
| NGC6334I | 0.90 | 0.14 | 17.66 | 1.13 |
| G35.2−0.7N | 0.18 | 0.07 | 2.17 | 0.60 |
| W75N | 1.01 | 0.15 | 8.71 | 1.27 |
| Non-detections | | | | |
| AFGL 437 | <0.15 | 0.05 | <1.20 | 0.40 |
| AFGL 5157 | <0.12 | 0.04 | <0.99 | 0.33 |
| G192.16−3.82 | <0.12 | 0.04 | <1.02 | 0.34 |
| GGD27-IRS1 | <0.24 | 0.08 | <1.95 | 0.65 |
| S88B | <0.24 | 0.08 | <1.95 | 0.65 |
| IRAS 19550+3248 | <0.15 | 0.05 | <1.20 | 0.40 |
| IRAS 20188+3928 | <0.24 | 0.08 | <1.98 | 0.66 |

lizing the RM01 sample is that they have a homogeneous dataset which has been analyzed in a consistent manner, making it a reliable database from which outflow parameters can be obtained.

The sample consists of 10 of the 11 sources studied by RM01 (the exception is NGC 6334-B) with the addition of two other sources which have been recently well studied: G192.16−3.82 (Shepherd et al. 1998) and G35.2−0.7N (Gibb et al. 2003). The mean distance for the sample is 1.9 ± 0.2 kpc. The sources are listed in Table 1, separated into detections and non-detections. The sources are described in turn in Section 3 below.

2 OBSERVATIONS AND MAPPING STRATEGY

The SiO $J=5 \rightarrow 4$ observations were carried out using the 15-m James Clerk Maxwell Telescope (JCMT) on Mauna Kea, Hawaii over the period 2000 July 29 to 2000 August 22. Table 1 lists the (0,0) positions for the sources observed. The positions represent

Table 3. Properties of the BIMA observations. The beam FWHM are denoted by θ_a and θ_b for the major and minor axes respectively, the position angle (PA) is in degrees east of north. The noise level per 1.4- km s^{-1} -wide channel is denoted by σ_{line} .

| Source | $\theta_a \times \theta_b$ (arcsec ²) | PA (degrees) | K/Jy | σ_{line} Jy/beam |
|-----------|--|-----------------|------|-----------------------------------|
| W3IRS5 | 21.3×19.0 | 76 | 0.41 | 0.13 |
| AFGL 5142 | 19.8×12.0 | 65 | 0.69 | 0.11 |
| W75N | 19.2×14.0 | 87 | 0.61 | 0.09 |

the location of the outflow driving source. The receiver was tuned to the SiO 5→4 line at 217.1050 GHz. The bandwidth was 500 MHz and spectral resolution 378 kHz (0.52 km s^{-1} at 217 GHz). The spectra were binned to a velocity resolution of 4.2 km s^{-1} to search for detections and for subsequent analysis. Calibration and pointing checks were carried out using W3(OH), W75N, G34.3 and IRAS 16293−2422. Pointing uncertainties were generally below 3 arcsec. The typical zenith system temperature was 370 K, and the noise level (ΔT_{MB}) was 50 mK in the binned spectra (Table 2 lists the noise for each source). The JCMT beam has a full-width at half-maximum (FWHM) of 22 arcsec at 217 GHz, matching the $J=2 \rightarrow 1$ CO observations of RM01. Line intensities were recorded as T_{A}^* , which have been converted to main-beam brightness temperatures, $T_{\text{MB}} = T_{\text{A}}^* / \eta_{\text{MB}}$ (where the main beam efficiency, η_{MB} , is 0.71 at 217 GHz).

The exact coverage for each source was determined by the size of the outflow (from RM01). In most cases an initial map was made, either a 7-point strip along the flow axis or a 3×3 grid of points. If SiO emission was detected, the map was extended with individual pointings to follow the CO emission (though some maps were extended in the case where no SiO emission was detected). The resulting coverage for each source is shown graphically in appendix A (Figs. A1 to A8).

In addition SiO $J=2 \rightarrow 1$ observations of AFGL 5142, W3-IRS5 and W75N were made with 9 antennas of the Berkeley-Illinois-Maryland Association (BIMA) interferometer at Hat Creek, CA over the period 2003 August 9 to 14. The array was in its most compact (D) configuration and in each case a 7-point

Table 4. Properties of the BIMA SiO 2→1 emission.

| Source | T_b (K) | σ (K) | $\int T_b dv$ (K km s ⁻¹) | σ (K km s ⁻¹) |
|------------|--------------|-----------------|--|-------------------------------------|
| W3IRS5 | 0.40 | 0.05 | 2.54 | 0.19 |
| AFGL 5142 | 1.55 | 0.08 | 13.14 | 0.42 |
| G35.2-0.7N | 0.16 | 0.06 | 1.70 | 0.18 |
| W75N | 2.05 | 0.05 | 17.38 | 0.26 |

hexagonal mosaic of pointings was made to improve sensitivity to extended structure. The resulting field of view was approximately 2.5 arcmin in diameter. Flux calibration was carried out using 3C84 and MWC349 assuming fluxes at 86 GHz of 4.0 and 1.0 Jy respectively, based on their flux histories derived from multiple planet observations. The phase calibrators were 0136+478, 3C111, and MWC349 with bootstrapped fluxes of 4.0 and 1.3 Jy respectively for the first two. The estimated relative calibration uncertainty is of order 10 per cent. The spectral resolution of the SiO observations was 1.4 km s⁻¹. Table 3 lists the parameters for the BIMA observations. Note that G35.2-0.7N was observed in the $J=2\rightarrow 1$ transition with BIMA (with slighter higher angular resolution) by Gibb et al. (2003).

3 RESULTS

Of the 12 sources observed, SiO 5→4 emission was detected in five: W3-IRS5, AFGL 5142, NGC 6334I, G35.2-0.7N and W75N. The detection criteria were a peak brightness temperature of at least 5- σ within the velocity extent of the outflow or an integrated intensity of at least 5- σ integrated over a 20- km s⁻¹ velocity range centred at the LSR velocity (since most of the detections are at or close to the LSR velocity). The emission is generally compact, peaking on or close to the location of the outflow driving source (see Figs. 1 and 2 for spectra). Extended 5→4 emission was detected towards W3-IRS5, NGC 6334I and G35.2-0.7N. The results are described in more detail in the following subsections. An overview is also given of all of the sources in the sample, primarily aimed at updating the discussion of RM01.

3.1 W3-IRS5

As mapped by RM01, the CO flow from W3-IRS5 extends for approximately 3.5 arcmin predominantly along a north-west to south-east axis (Fig. A1). An earlier map published by Mitchell, Maillard & Hasegawa (1991) showed only a compact NE-SW flow, although they integrated over a different velocity range. W3-IRS5 was not detected in the SiO survey of maser sources by Harju et al. (1998). Tieftrunk et al. (1995) derived a mass of $\sim 800 M_\odot$ for the core containing W3-IRS5.

The SiO $J=5\rightarrow 4$ emission peaks strongly on IRS5 (see Fig. 3a), and is extended in an east-west direction rather than following the larger-scale CO flow. Though not immediately obvious, this east-west component is also seen in the CO map of RM01: approximately 35 arcsec east of IRS5, there is a peak of red- and blue-shifted CO emission, and the contours of the blue lobe show an extension to the west.

The BIMA data show this east-west flow more clearly, with the SiO $J=2\rightarrow 1$ emission extending for approximately 90 arcsec (Fig. 3b). Three clear maxima are present, the two strongest of which peak east and west of IRS5 itself. This suggests that the east-

west flow is the main outflow driven by W3-IRS5. The larger-scale flow may be from one of the other sources in this region.

The $J=5\rightarrow 4$ centre spectrum (Fig. 1a) has a symmetric appearance, with a FWHM linewidth of 6.2 km s⁻¹ and no evidence for non-Gaussian wings. Similarly the 2→1 lines are also symmetric (Fig. 2a), but there is a gradient in peak velocity from east to west. The east peak is red-shifted by ~ 1.5 km s⁻¹ relative to the rest velocity, with the western peaks blue-shifted by 1.5 (near) and 2 km s⁻¹ (far), in the same sense as the CO lobes. Linewidths of the 2→1 lines range from 5 (east peak) to 8 km s⁻¹ (near west peak).

3.2 AFGL 5142

The CO flow from AFGL 5142 is orientated in a north-south direction and shows two strong compact components with weaker extended emission (RM01: see also Fig. A2). Hunter et al. (1999) observed the 2→1 transition of SiO (with higher resolution than the BIMA observations presented here) and detected a bipolar jet extending for approximately 30 arcsec. The outflow is also seen in HCO⁺ (Hunter et al. 1999). Hunter et al. (1999) derived a mass of $\sim 145 M_\odot$ for the core housing the outflow driving source. Ammonia observations by Zhang et al. (2002) reveal a compact and slightly extended structure perpendicular to the main CO outflow direction. More recent work by Zhang et al. (2007) shows that there may be a number of outflows in this region. The close superposition of the red and blue lobes along with the elongated core and bipolar jet geometry suggests that the outflow from AFGL 5142 lies close to the plane of the sky.

The JCMT map of AFGL 5142 is shown in Fig. 4a and is dominated by a single peak centred a few arcsec north of the central source. The emission also shows evidence for a slight extension to the north-east but confirmation requires more extensive mapping. The JCMT spectrum shown in Fig. 1b is symmetric and centred at the systemic velocity, with no clear evidence of red or blue wings. The FWHM is 7.9 km s⁻¹.

The BIMA SiO 2→1 data show a more collimated appearance, in good agreement with the results of Hunter et al. (1999). The blue and red-shifted emission is largely coincident (Fig. 4), both peaking at the source position. The red lobe has a second distinct maximum 20 arcsec to the north, which coincides with the main red lobe seen by Hunter et al. (1999). The blue lobe shows an elongation to the north-east which is not seen by Hunter et al., suggesting that the lower-resolution observations may be detecting a weak extended component. The centre spectrum (shown in Fig. 2b) has a FWHM of 7.5 km s⁻¹, in good agreement with the 5→4 line.

3.3 NGC 6334I

The CO outflow from NGC 6334I shows two compact lobes separated by ~ 40 arcsec, red-shifted to the north-east and blue-shifted to the south-west (RM01, see also Leurini et al. 2006 and Fig. A3). A second flow is present ~ 30 arcsec north-west of NGC 6334I but the SiO mapping did not extend far enough to cover it. Harju et al. detected 2→1 and 3→2 emission towards NGC 6334I. McCutcheon et al. (2000) present a detailed study of this region, and estimate the mass of the core housing NGC 6334I to be $\sim 200 M_\odot$. Recent high-resolution mapping by Hunter et al. (2006) resolves this core into four protostellar condensations each with a mass of a few tens of solar masses.

The SiO 5→4 emission from NGC 6334I has the broadest

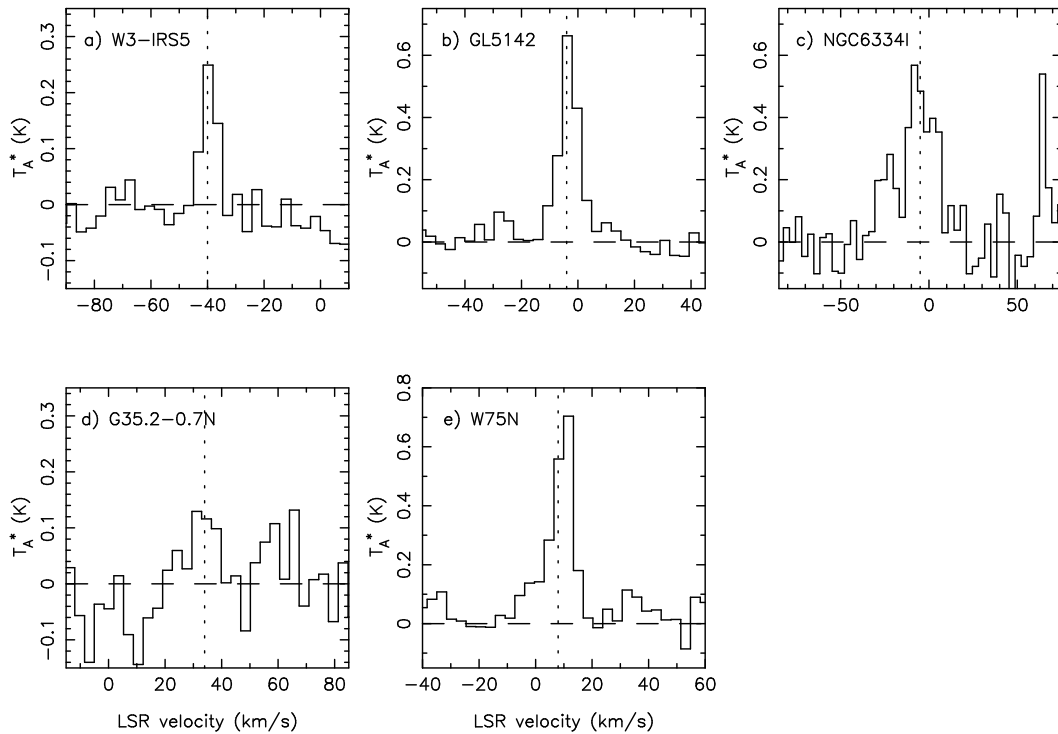


Figure 1. SiO $J=5 \rightarrow 4$ spectra from the centre position of each detected source. The vertical dashed line in each panel marks the systemic velocity as given in Table 1.

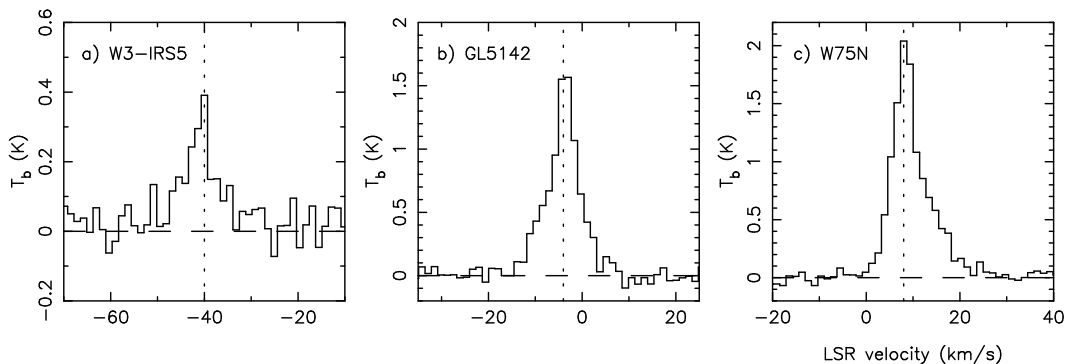


Figure 2. SiO $J=2 \rightarrow 1$ spectra from the peak position of each detected source. The spectra are averages over approximately one beam area. The vertical dashed line in each panel marks the systemic velocity as given in Table 1.

lines of all detections with a FWHM of 20 km s^{-1} (see Fig. 1c). Fig. 5a shows the integrated intensity across the whole velocity range (-40 to $+40 \text{ km s}^{-1}$). It is the only source with significant extended $5 \rightarrow 4$ emission, which extends along the axis of the CO flow. The distribution of red- and blue-shifted SiO emission matches that of the CO. Fig. 5b shows the red- and blue-shifted SiO lobes. Also the SiO peaks behind the H_2 knots seen by Davis & Eislöffel (1995), supporting a shock origin for the SiO.

None of the spectra is symmetric or gaussian in shape; no attempts therefore have been made to fit gaussians. The spectrum at the centre position (Fig. 1c) shows maybe 3 velocity components: one blue-shifted at -17 km s^{-1} relative to the systemic velocity, the strongest component near the systemic velocity and a red-shifted component at $+8 \text{ km s}^{-1}$, suggesting there are SiO clumps in the flow. In the lobes of the outflow, the SiO $5 \rightarrow 4$ spectra peak

near the rest velocity and exhibit a monotonically-decreasing blue wing extending to $\sim 30 \text{ km s}^{-1}$ relative to the systemic velocity.

3.4 G35.2–0.7N

The CO outflow from G35.2–0.7N extends for ~ 2 arcmin either side of the driving source (Gibb et al. 2003; Fig. A4). In addition to this large-scale flow (with position angle of 65 degrees east of north) there is a compact north-south jet-like flow, probably driven by the radio jet source (Gibb et al. 2003; Birks, Fuller & Gibb 2006). Gibb et al. (2003) derived a mass of $\sim 800 M_{\odot}$ for the core containing G35.2–0.7N.

G35.2–0.7N is the weakest SiO $5 \rightarrow 4$ detection in this sample, at only $2.5\text{-}\sigma$ in intensity and $3.6\text{-}\sigma$ in integrated intensity. This detection appears to be genuine since more sensitive observations yield a line intensity in good agreement with the data presented

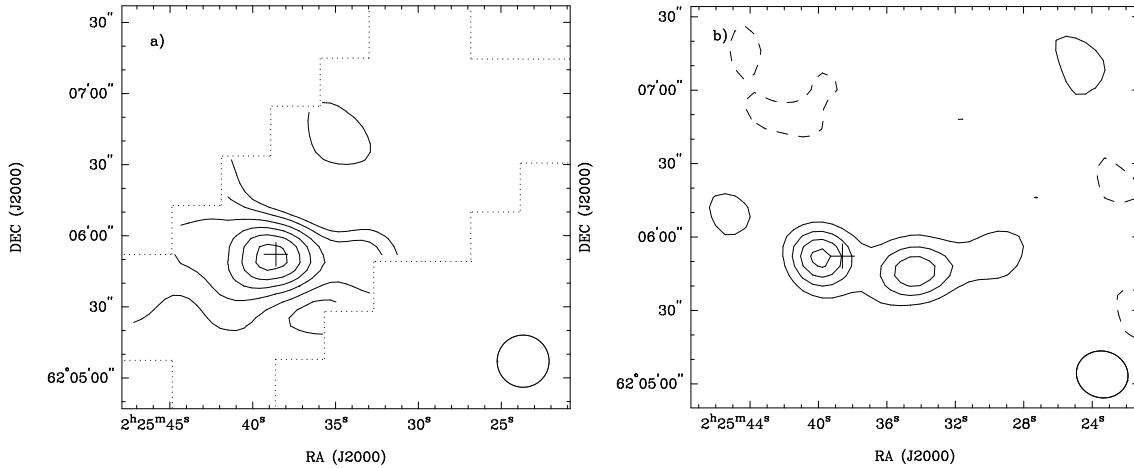


Figure 3. W3-IRS5: a) SiO $J=5\rightarrow 4$ and b) $J=2\rightarrow 1$ integrated intensity between ± 5 km s $^{-1}$ relative to the line centre. The cross marks the location of the YSO. Contours are at a) $-0.4, 0.4, 0.7, 1.1, 1.4, 1.8, 2.1$ K km s $^{-1}$ and b) $-0.5, 0.5, 1.1, 1.7, 2.2$ K km s $^{-1}$ respectively. The dotted lines in the $5\rightarrow 4$ map denote the region mapped with the JCMT.

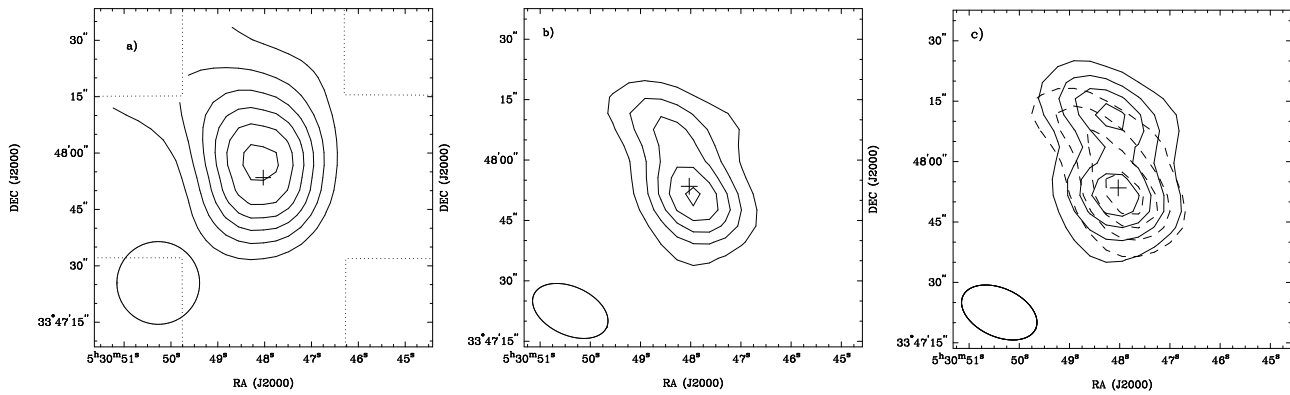


Figure 4. AFGL 5142: a) SiO $J=5\rightarrow 4$ and b) $J=2\rightarrow 1$ integrated intensity over the velocity range ± 10 km s $^{-1}$. Contours are at a) $-1.3, 1.3, 2.5, 3.8, 5.1, 6.3, 7.6$ K km s $^{-1}$ and b) $-2.5, 2.5, 5.0, 7.5, 10.0, 12.5$ K km s $^{-1}$ respectively. The cross in each panel marks the continuum peak. Small dots mark the position of water masers from Hunter et al. (1999). c) Blue- (dashed contours) and red-shifted (solid contours) $J=2\rightarrow 1$ emission from between 0 and ± 5.4 km s $^{-1}$ relative to the rest velocity. Contours start at $-1.5, 1.5, 3.0, 4.5, 6.0, 7.5$ K km s $^{-1}$ in each lobe. The dotted lines in the $5\rightarrow 4$ map denote the region mapped with the JCMT.

here (Gibb et al. 2003). Figure 1d shows the spectrum recorded at the central position. The emission covers a velocity extent of ~ 10 km s $^{-1}$. The $5\rightarrow 4$ integrated intensity map is shown in Fig. 6. The emission peaks on the central core housing G35.2N and G35MM2, extending slightly to the south.

SiO $J=2\rightarrow 1$ data observed with BIMA are shown in Gibb et al. (2003). To summarize, the SiO $2\rightarrow 1$ emission shows some similarity with the $5\rightarrow 4$ emission in Fig. 6, peaking at the outflow centre and extending south. The $2\rightarrow 1$ emission also shows a limb of emission extending to the west into the red-shifted lobe of the large-scale outflow. This may be due to a separate flow unrelated to the CO, or could arise in a shocked shell along the inside of the outflow cavity (Gibb et al. 2003).

3.5 W75N

The CO outflow from W75N extends for approximately 3 arcmin, with the strong red lobe dominating the appearance (RM01; Davis, Smith & Moriarty-Schieven 1998; Fig. A5). The blue lobe is more compact, peaking close to the central cluster of sources (Shepherd 2001). Harju et al. (1998) detected the SiO $2\rightarrow 1$ line to-

wards W75N (called W75-OH in their paper). High-resolution SiO $1\rightarrow 0$ and $2\rightarrow 1$ imaging by Shepherd, Kurtz & Testi (2004b) revealed a bipolar distribution of red- and blue-shifted gas in the same sense as the CO flow. The $2\rightarrow 1$ emission peaks ~ 8 arcsec to the south/south-west of the cluster of radio sources at the outflow centre. No SiO emission was detected behind the sweeping bows at the end of the CO flow. Davis et al. (2007) present a SCUBA map of W75N although they do not calculate a mass from their measurements. Assuming a dust temperature of 50 K, the mass is $\sim 350 M_{\odot}$ (Hildebrand 1983).

The JCMT SiO map is shown in Fig. 7a and peaks at the outflow centre, coincident with the location of MM1 (Shepherd 2001). There is no extended emission despite the map covering the entire length of the CO flow. The spectrum at the centre position (Fig. 1e) is the brightest in this survey ($T_{\text{MB},54} \sim 1$ K). The line is largely symmetric though slightly red-shifted. There is also weak evidence of a blue-shifted wing. The FWHM of the emission is 7.9 km s $^{-1}$.

Similarly, the BIMA map (Fig. 7b) shows only a single well-defined maximum although in this case it is offset into the red lobe of the outflow by ~ 10 arcsec. This offset is in good agreement with the position of the peak emission seen in the higher-resolution $2\rightarrow 1$

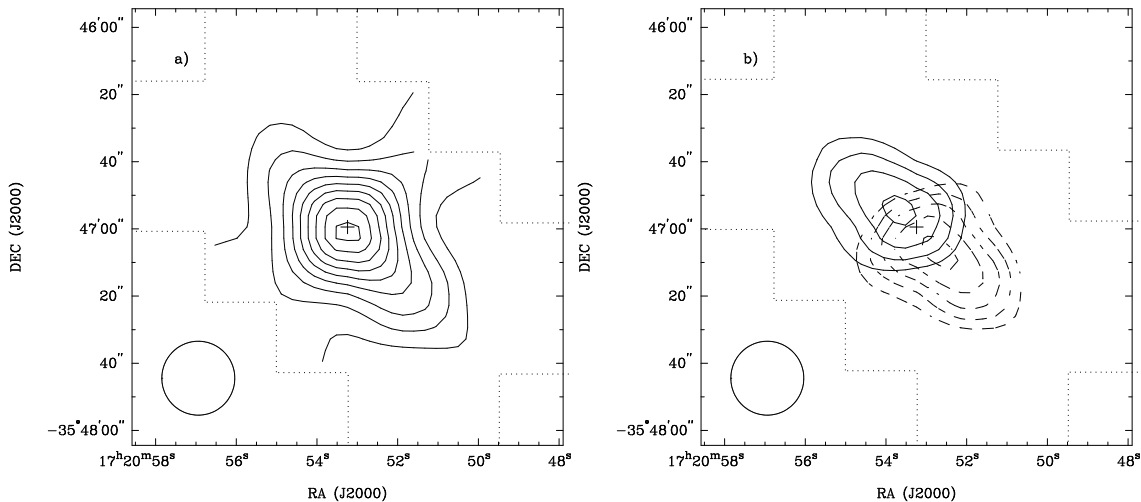


Figure 5. NGC 6334I: a) $J=5\rightarrow 4$ integrated intensity over the range -25 to $+12$ K km s^{-1} . Contours begin at 2.0 K km s^{-1} and increase in steps of 2.0 K km s^{-1} . b) Blue- (dashed contours) red-shifted (solid contours) lobes over the ranges -30 to -5 and $+5$ to $+30$ K km s^{-1} respectively. Contours begin at $2.0/1.5$ K km s^{-1} in the red and blue lobes respectively and increase in steps of 0.5 K km s^{-1} . The cross in each panel marks the position of NGC 6334I. The dotted lines denote the region mapped with the JCMT.

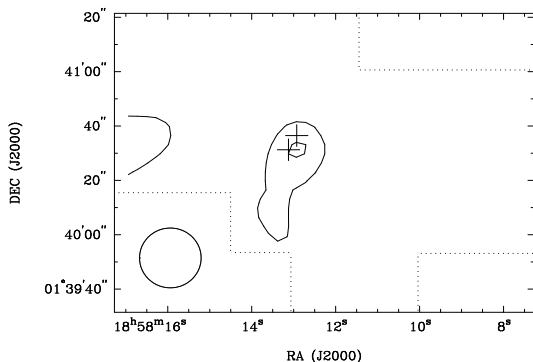


Figure 6. G35.2–0.7N: $J=5\rightarrow 4$ integrated intensity over the range ± 10 K km s^{-1} . Contours are at 0.7 and 1.0 K km s^{-1} . The crosses mark the locations of the sources G35.2N (centre) and G35MM2 (bottom-left). The dotted lines denote the region mapped with the JCMT.

map of Shepherd et al. (2004b). The difference in peak position for the $2\rightarrow 1$ and $5\rightarrow 4$ emission is probably due to pointing errors. The spectrum at the peak (Fig. 2c) shows a pronounced red wing extending to ~ 12 K km s^{-1} from the systemic velocity. However, there is no evidence for emission from individual outflow lobes. The $2\rightarrow 1$ line has a peak brightness temperature of 2 K , considerably higher than the detection of Harju et al. (1998), probably due to the smaller beam of the BIMA observations.

3.6 Non-detections

What about the non-detections? It is not likely that this study is biased by uneven noise levels because most of the sources observed under the noisiest conditions were detected. Only one $5\rightarrow 4$ non-detection was detected previously: IRAS 20188+3928 was detected in the $2\rightarrow 1$ transition by Harju et al. (1998). The non-detection of the $5\rightarrow 4$ transition is perhaps surprising given that the outflow was detected in $1\rightarrow 0$ and $3\rightarrow 2$ HCO^+ (Little et al. 1988).

The one source in the sample of RM01 that was not observed in this survey is NGC 6334B. However, Harju et al. (1998) detected

strong emission from this source in both the $2\rightarrow 1$ and $3\rightarrow 2$ transitions, and it is thus possible that this source would have been detected in the current experiment.

3.6.1 AFGL437

Recently mapped in C^{18}O by Saito et al. (2007), AFGL 437 is embedded in a molecular cloud of mass at least $1500 M_{\odot}$, although the gas does not peak close to the infrared cluster. It is likely that the immediate environment of AFGL 437 contains a few hundred solar masses of material. Harju et al. (1998) also did not detect AFGL 437 in SiO.

3.6.2 AFGL 5157

Kumar, Keto & Clerkin (2006) found a compact (~ 1 pc diameter) cluster of near-infrared sources associated with this region. Klein et al. (2005) mapped AFGL 5157 at $850 \mu\text{m}$ and found that the centre of the cluster was devoid of emission. Instead their mapping showed that the dust is associated with the outflow source, the strongest peak lying at the centre of the red and blue lobes. Fontani et al. (2006) derived a mass of $179 M_{\odot}$ for this core.

3.6.3 G192.16–3.82

This region is now known to contain at least three sources, two of which appear to be low-mass YSOs (Shepherd et al. 2004a). Kumar et al. (2006) found a compact cluster of near-IR objects. Shepherd et al. (2004a) derived a mass of $75 M_{\odot}$ from submillimetre dust observations, similar to the value of $117 M_{\odot}$ derived from C^{18}O by Shepherd & Kurtz (1999). Harju et al. (1998) also did not detect SiO towards G192.16–3.82.

3.6.4 GGD27-IRS1

Also known as the outflow source HH 80–81. VLA and BIMA imaging by Gómez et al. (2003) revealed a compact core with a temperature < 50 K . Submillimetre continuum imaging with

SCUBA by Thompson et al. (2006) showed marginally-extended emission perpendicular to the outflow axis. The mass estimated from the 850 μm flux density is $\sim 200 M_{\odot}$ assuming a temperature of 50 K.

3.6.5 S88B

Little studied since RM01, but also mapped in C^{18}O by Saito et al. (2007) who found four clumps with masses in the range 50–450 M_{\odot} . The most massive of these is associated with S88B.

3.6.6 IRAS 19550+3248

Almost no further work has been done on this source since the CO study by Koo et al. (1994). The properties are very poorly known, Koo et al. (1994) estimating a core mass of $\sim 220 M_{\odot}$. A similar value for the virial mass may be derived from the CS detection by Bronfman, Nyman & May (1996) assuming the core is the same size as the beam of their observations.

3.6.7 IRAS 20188+3928

This source was mapped in HCO^+ by Little et al. (1988) who discovered that, like AFGL 5142 above, the outflow was dense enough to excite HCO^+ . Later Anglada, Sepulveda & Gómez (1997) mapped the ammonia emission and derived a mass of $\sim 800 M_{\odot}$ (assuming a distance of 2 kpc: the distance to this object is not well-constrained). In their large-scale survey of the Cygnus X region, Schneider et al. (2006) mapped the core associated with this source in ^{13}CO , showing that it is associated with a well-defined enhancement in the ^{13}CO emission.

4 ANALYSIS

The data were analyzed in two ways. The first assumed that the emission was optically thin, and that the level populations were in local thermodynamic equilibrium (LTE) which could be characterized by a single temperature. For the sources in which two transitions were observed, radiative transfer modelling was employed to provide an independent estimate of the SiO abundance and to estimate the properties of the SiO-emitting regions.

4.1 LTE analysis

The beam-averaged SiO column densities were calculated using the following formula (from Irvine et al. 1987):

$$N_{\text{SiO}} = \frac{1.94 \times 10^3 \nu^2}{f_J A_{J,J-1}} \int T dv, \quad (1)$$

where ν is the frequency (GHz), $A_{J,J-1}$ is the spontaneous emission coefficient (s^{-1}), f_J is the fraction of molecules in level J , N_{SiO} is the total SiO column density (cm^{-2}) and $\int T dv$ is the integrated intensity (K km s^{-1}). The SiO emission probably arises from regions much smaller than the JCMT beam and so the main-beam brightness temperatures are used in the calculations. For the BIMA data conversion was from Jy beam $^{-1}$ to K for an equivalent CLEAN beam brightness temperature (see Table 3).

Since we have no estimates of the excitation temperatures, we assume a value of 75 K for both transitions. For temperatures in the range 50 to 100 K (see § 4.2) the uncertainty introduced by an

unknown excitation temperature is only ~ 20 per cent, increasing to ~ 50 per cent at a temperature of 25 K. The values of A_{21} and A_{54} are calculated as $2.92 \times 10^{-5} \text{ s}^{-1}$ and $5.20 \times 10^{-4} \text{ s}^{-1}$ respectively (see e.g. Irvine et al. 1987; Ziurys et al. 1989). Table 5 lists the SiO column densities for sources with detected SiO 2→1 and/or 5→4 emission.

The SiO column densities derived from the 5→4 line range from $\sim 4 \times 10^{12}$ up to $3 \times 10^{13} \text{ cm}^{-2}$. Values derived from the 2→1 line are 3–8 times higher. These are similar in magnitude to the values derived for low-luminosity sources in Paper I and other studies (e.g. Blake et al. 1995; Garay et al. 1998). They are also similar to values in a number of high-mass sources (e.g. Acord et al. 1997; Miettinen et al. 2006). Converting these to abundances requires choice of a H_2 column density. This is problematic since such estimates are not necessarily available for the sources in the current sample. SiO abundances are discussed further in Section 4.3 below.

4.2 Radiative transfer modelling

With two transitions it is possible to constrain some of the properties of the emitting gas. Here the same radiative transfer model as was used in Paper I is applied, which assumes a uniform spherical cloud, statistical equilibrium and makes the Large Velocity Gradient (LVG) approximation (Goldreich & Kwan 1974). Collision rates were taken from Turner et al. (1992). The parameter space covered by the modelling extends from a H_2 number density of 10^4 cm^{-3} to 10^9 cm^{-3} and a kinetic temperature of 20 to 150 K. The third variable is the ratio of the abundance to the velocity gradient, $X/(dv/dr)$ (see e.g. Paper I). Therefore a velocity gradient must be assumed in order to derive an abundance. In the absence of any other information, the velocity gradient was taken to be the FWHM linewidth of the SiO line divided by the beam diameter. While the precise value for the length term in the velocity gradient is perhaps somewhat arbitrary, the solutions scale linearly with the choice of value and thus can be amended trivially. The FWHM linewidth was 6, 8, 10 and 8 km s^{-1} for W3-IRS5, AFGL 5142, G35.2–0.7N and W75N respectively resulting in the velocity gradients shown in Table 6. Using these values translates $X/(dv/dr)$ into an abundance range for SiO of between $\sim 10^{-11}$ and $\sim 10^{-7}$ relative to H_2 .

Table 6 summarizes the parameters for the best-fitting solutions (given for a representative temperature of 100 K), also shown graphically in Fig. 8a–d. The 5→4/2→1 ratio constrains the density quite well and is only weakly dependent on temperature with lower-density/higher-abundance solutions occurring at higher temperatures. However, the temperature itself is not well-constrained over the entire range 50–150 K. It should be noted that the solutions plotted in Fig. 8 represent lower limits to the abundance, because the filling factor of the 5→4 transition will be lower than that of the 2→1. The corresponding SiO column densities lie in the range 6×10^{12} to $4.5 \times 10^{14} \text{ cm}^{-2}$, in good agreement with the LTE values given in Table 5.

4.3 SiO abundances

The abundances derived from the LVG modelling (Table 6) are in reasonable agreement, if slightly higher than, estimates in comparable sources (e.g. Miettinen et al. 2006). Note that Gibb et al. (2003) did not draw any firm conclusions regarding the modelling for G35.2–0.7N, although they did not rule out a high density/low abundance solution ($10^6 \text{ cm}^{-3}/10^{-11}$ respectively).

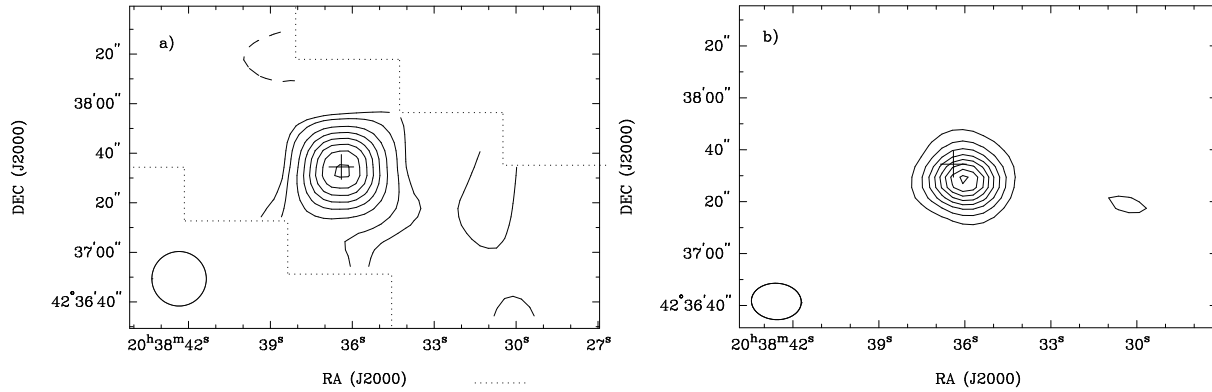


Figure 7. W75N: SiO $J=5\rightarrow 4$ and b) $J=2\rightarrow 1$ integrated intensity over the velocity range $\pm 10 \text{ km s}^{-1}$. Contours are at a) $-0.7, 0.0, 0.7, 1.4, 2.8, 4.2, 5.6, 7.0, 8.4 \text{ K km s}^{-1}$ and b) $-1.3, 1.3, 2.6, 4.0, 5.3, 6.6, 7.9, 9.2, 10.6 \text{ K km s}^{-1}$ respectively. The cross in each panel marks the continuum peak. The dotted lines in the $5\rightarrow 4$ map denote the region mapped with the JCMT.

Table 5. LTE column densities and abundances derived from the $2\rightarrow 1$ and $5\rightarrow 4$ transitions. See the text for a description of how the H_2 column density was derived. The uncertainties are based on the $1\text{-}\sigma$ uncertainties quoted in Tables 2 and 4. The uncertainty in the abundance includes the range of values derived from the $2\rightarrow 1$ and $5\rightarrow 4$ data. The notation $a(b)$ represents $a \times 10^b$.

| Source | $N_{\text{SiO}(2\rightarrow 1)}$ (cm^{-2}) | $N_{\text{SiO}(5\rightarrow 4)}$ (cm^{-2}) | N_{H_2} (cm^{-2}) | X_{SiO} (outflow) |
|------------|--|--|--|-------------------------------|
| W3-IRS5 | $1.8 \pm 0.1(13)$ | $4.2 \pm 0.6(12)$ | 1.2(19) | 0.3–1.5(–6) |
| AFGL 5142 | $9.4 \pm 0.3(13)$ | $1.4 \pm 0.1(13)$ | 2.9(19) | 0.5–3.2(–6) |
| NGC6334I | – | $3.1 \pm 0.2(13)$ | 1.1(20) | $2.8 \pm 0.2(–7)$ |
| G35.2–0.7N | $1.2 \pm 0.1(13)$ | $3.8 \pm 1.1(12)$ | 1.5(18) | 2.5–8.0(–6) |
| W75N | $1.2 \pm 0.1(14)$ | $1.5 \pm 0.2(13)$ | 6.3(18) | 0.2–1.9(–5) |

Table 6. Summary of LVG modelling. The brightness temperatures for the $2\rightarrow 1$ and $5\rightarrow 4$ transitions and assumed velocity gradients are given in columns 2–5. The parameter range for the solutions is given in columns 6 and 7 and values are quoted for a representative kinetic temperature of 100 K. The notation $a(b)$ represents $a \times 10^b$.

| Source | T_{21} (K) | T_{54} (K) | T_{54}/T_{21} | dv/dr ($\text{km s}^{-1} \text{ pc}^{-1}$) | n_{H_2} (cm^{-3}) | X_{SiO} |
|------------|-----------------|-----------------|-----------------|---|--|------------------|
| W3IRS5 | 0.40 | 0.37 | 0.9 | 27 | 0.6–2.0(5) | 2.0–6.0(–10) |
| AFGL 5142 | 1.55 | 0.92 | 0.6 | 47 | 0.4–1.5(5) | 0.8–3.0(–9) |
| G35.2–0.7N | 0.16 | 0.18 | 1.1 | 47 | 0.7–2.0(5) | 1.0–4.0(–10) |
| W75N | 2.05 | 1.01 | 0.5 | 42 | 0.4–1.0(5) | 1.5–7.0(–9) |

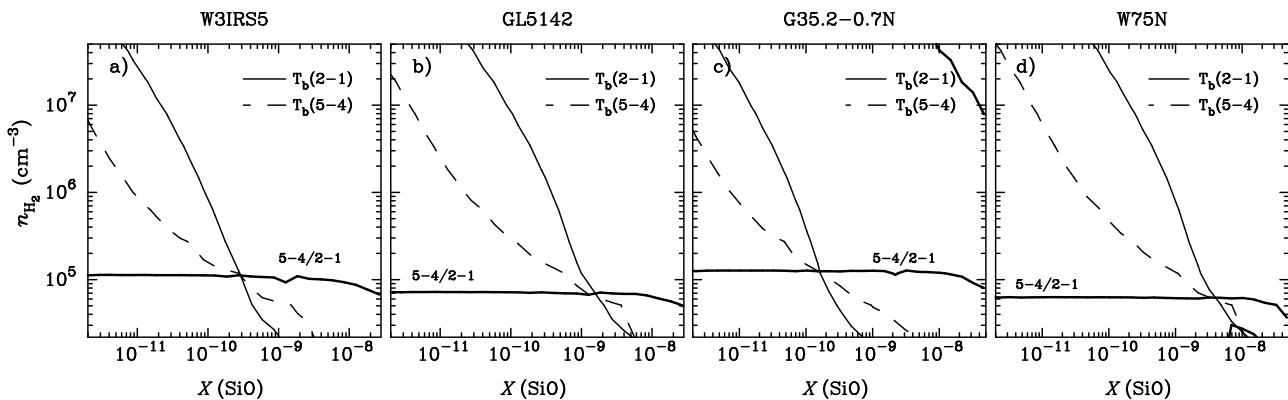


Figure 8. LVG solutions. The locus of LVG solutions giving the observed $2\rightarrow 1$ and $5\rightarrow 4$ brightness temperatures (and their ratio) is plotted as a function of H_2 number density and SiO abundance. The kinetic temperature is fixed at 100 K for all panels. Higher (lower) temperatures yield lower (higher) densities within a factor of 2–3 of those in this plot. Note the nominal solution lies at the intersection of the lines of constant brightness temperature. The ratio is derived from these and thus that contour line is guaranteed to pass through the same point. However, due to incomplete beam filling, the solution represents a lower limit to the estimate of the abundance.

To derive LTE abundances an estimate of the H₂ column density is needed. For the majority of detected sources the SiO emission is clearly associated with the outflow. Therefore it seems justifiable to estimate the H₂ column density in the flow from the CO properties (as used in Paper I.) The mean H₂ column density within the outflow was estimated from $N_{\text{H}_2} \propto M_{\text{out}}/l^2$ where M_{out} is the outflow mass (corrected for optical depth) and l is the outflow size (see Table 7 below). In all sources the 2→1 transition yielded a larger abundance than the 5→4 line, by as much as an order of magnitude. This may be a reflection of different filling factors for each line, since the 2→1 line is excited in less dense gas than the 5→4. The highest abundance was obtained for W75N at 2×10^{-5} relative to H₂ (from the 2→1 emission). This is close to the cosmic abundance of Si (2.5×10^{-5}) and would imply almost complete destruction of the dust grains and subsequent conversion of Si to SiO.

The LTE abundances in Table 5 are much higher than those derived from the LVG modelling, and also higher than the typical values for low-mass outflow sources (e.g. Blake et al. 1995, Garay et al. 1998, Hirano et al. 2001, Garay et al. 2002, Paper I). The exceptions are W3-IRS5 and AFGL 5142 which have abundances derived from the 5→4 line which are comparable with the values derived for L1448-mm and HH211-mm in Paper I. Estimates for comparable high-mass sources range from a few $\times 10^{-10}$ (Peng, Vogel & Carlstrom 1995; Miettinen et al. 2006) up to $\sim 10^{-7}$ (Ziurys & Friberg 1987; Shepherd, Churchwell & Wilner 1997), though most of these estimates use H₂ column densities from ambient gas tracers rather than the outflow.

However, given the good agreement between the LTE- and LVG-derived SiO column densities, it would seem that deriving N_{H_2} from the outflow mass is perhaps not a robust method for estimating SiO abundances, and tends to significantly over-estimate the SiO abundance. While the SiO appears to be clearly associated with the outflow, it is also evident that the SiO and CO are not well-mixed: most of the outflow shows CO emission with no corresponding SiO. Furthermore, the bulk of the SiO emission occurs at velocities similar to the systemic velocity, rather than at high velocities. Lastly, the outflow masses are themselves lower limits due to the choice of low-velocity cut-off (RM01, Masson & Chernin 1994). Increased outflow masses will result in higher H₂ column density and thus lower SiO abundances.

5 DISCUSSION

In the current study, 5 of 12 (42 per cent) sources were detected. For the sources in the RM01 survey alone, the detection rate is 4 out of 10 (40 per cent).

In their sample, Harju et al. (1998) found that for the more luminous sources (with luminosities exceeding $10^4 L_{\odot}$), the detection rate was of order 45 per cent, in good agreement with the detection rate in the current study. The median and mean luminosities are also $\sim 1-2 \times 10^4 L_{\odot}$. Including sources above $10^3 L_{\odot}$ the Harju et al. detection rate drops to 38 per cent, but still in close agreement with the current result. It should be stressed that the current sample is quite small and therefore the statistics are relatively poor. A larger sample is clearly desirable.

5.1 Factors determining SiO emission

In order to investigate the possible factors which might determine whether or not SiO emission is detected, the SiO 5→4 luminosity has been plotted as a function of various source and outflow

properties. Table 7 lists the relevant properties which are shown in Fig. 9. Most of these values were taken from RM01 with the exception of G192.16–3.82 and G35.2–0.7N which were taken from Shepherd et al. (1998) and Gibb et al. (2003) respectively. The only property derived here is a mean outflow density, n_{out} , defined as $M_{\text{out}}/(2.3m_{\text{H}}V_{\text{out}})$ (where V_{out} is the total volume of the two outflow lobes, $V_{\text{out}} = \pi r^3/3$ where $r = l/2$ and l is given in Table 7). The reason for examining this parameter is that it is assumed that an outflow with a high mean density reflects a denser ambient medium. Since the SiO 5→4 transition requires a high density to excite, it might be expected that denser environments promote greater emission (although see § 5.2.4 in Paper I for a counter-argument regarding the depletion timescale in shocked gas). However, it should be noted that these densities are only meant to be taken as representative values since the actual geometry of the CO is not known, and therefore should not be directly compared with the densities derived from the LVG modelling.

For the most part there are no clear correlations between the outflow and/or source parameters and the SiO 5→4 luminosity. The exception is the outflow velocity range (full width at zero intensity), plotted in Fig. 9a. In four out of the five cases, detected sources have higher velocities than those which were not detected. The exception is AFGL 5142, the outflow from which lies close to the plane of the sky which would lead to an underestimate of the outflow velocity. Treating the detections and non-detections as independent sub-samples, the mean total velocity range for the detected sub-sample is significantly greater (3σ) than that for the non-detected sub-sample.

No other relationships are evident in Fig. 9b–f, and in most cases there is no significant difference in the mean values of the other parameters for the detected and non-detected sub-samples. There are of order 1σ differences between the mean detected/non-detected outflow densities and source luminosities. Codella et al. (1999) found a correlation between source luminosity and SiO emission in their sample. As with the low-mass sources in Paper I, no significant correlation is evident for the massive YSOs in the current sample (Fig. 9f). However, the mean source luminosity for the SiO-detected subsample is greater than that for the non-detections (although only at the 1σ level). Thus there is a suggestion that higher luminosity sources and sources with denser outflows may also be more likely to be detected.

The observed outflow velocity (along with several other outflow parameters) is highly dependent on outflow viewing angle. If there were no dependence on velocity, then the detections and non-detections would be well mixed, as is evident in the plots of the outflow momentum flux and mechanical luminosity. However, the velocities are clearly not uniformly distributed, which means that the correlation seen in Fig. 9a is genuine, unless the detected sources all have more favourable viewing angles than the non-detections (which does not appear to be the case).

5.2 Where is the SiO located?

As also noted by Harju et al. (1998), the SiO 5→4 spectra shown in Fig. 1 generally lie at the systemic velocity and appear symmetric with no clear wings as would be expected if the emission was associated with the leading bow-shock of an outflow. Could this imply that the SiO is not from the outflow at all, and that the emission arises from dense ambient gas? The LVG-derived abundances, while smaller than the LTE values are still greater than the canonical SiO abundance in ambient gas ($\sim 10^{-12}$ – Irvine et al. 1987; Ziurys et al. 1989). Furthermore, the SiO linewidths are larger than

Table 7. Outflow properties plotted in Figure 9. The SiO $J=5\rightarrow 4$ luminosity was calculated from the brightest emission where detected. Upper limits (quoted as $3\text{-}\sigma$) for non-detections were derived from the RMS noise level in a 20-km s^{-1} -wide range. The maximum velocity in a single outflow lobe is denoted by v_{max} , while the total maximum velocity extent of the outflow (both lobes) is Δv_{max} . The remaining parameters are all taken from RM01 with the exception of G192.16–3.82 Shepherd et al. 1998) and G35.2–0.7N (Gibb et al. 2003). The outflow size, l , is typically the mean maximum extent of the red and blue lobes. As described in the text, the outflow density is the outflow mass divided by the cube of the outflow size. The average properties are quoted with an error equal to σ/\sqrt{n} , i.e. the error on the mean of sample of n sources. The notation $a(b)$ represents $a \times 10^b$.

| Source | $L_{\text{SiO}5\rightarrow 4}$ (L_{\odot}) | v_{max} (km s^{-1}) | Δv_{max} (km s^{-1}) | dp/dt ($M_{\odot} \text{ km s}^{-1} \text{ yr}^{-1}$) | L_{mech} (L_{\odot}) | L_{bol} (L_{\odot}) | M_{out} (M_{\odot}) | l (pc) | n_{out} (cm^{-3}) |
|----------------|---|--|---|--|--------------------------------------|-------------------------------------|-------------------------------------|---------------|--|
| Detections | | | | | | | | | |
| W3-IRS5 | 3.0(−7) | 26 | 47 | 7.6(−1) | 2594 | 1.1(6) | 2016 | 1.73 | 5.3(4) |
| AFGL 5142 | 6.2(−7) | 13 | 23 | 1.1(−2) | 5.4 | 3.8(3) | 1082 | 0.80 | 2.9(5) |
| NGC6334I | 1.3(−6) | 47 | 80 | 7.7(−2) | 71.9 | 8.0(4) | 3317 | 0.74 | 1.1(6) |
| G35.2–0.7N | 2.2(−7) | 34 | 45 | 1.6(−3) | 3.5 | 2.0(4) | 12 | 0.74 | 4.1(3) |
| W75N | 8.6(−7) | 39 | 62 | 3.5(−2) | 46.4 | 1.4(5) | 548 | 1.23 | 4.0(4) |
| Average: | $6.6 \pm 1.8(-7)$ | 31.8 ± 5.2 | 51.4 ± 8.5 | $1.7 \pm 1.3(-1)$ | 540 ± 460 | $2.7 \pm 1.9(5)$ | 1400 ± 520 | 1.1 ± 0.2 | $3.0 \pm 1.8(5)$ |
| Non-detections | | | | | | | | | |
| AFGL 437 | $<1.2(-7)$ | 14 | 23 | 2.4(−1) | 750 | 2.4(4) | 620 | 1.36 | 3.3(4) |
| AFGL 5157 | $<7.8(-8)$ | 15 | 27 | 1.3(−1) | 217 | 5.5(3) | 672 | 0.69 | 2.8(5) |
| G192.16–3.82 | $<5.1(-8)$ | 15 | 31 | 3.0(−3) | 2.1 | 3.3(3) | 82 | 1.45 | 3.7(3) |
| GGD27-IRS1 | $<1.3(-7)$ | 10 | 18 | 1.5(−2) | 15.8 | 2.0(4) | 407 | 1.44 | 1.9(4) |
| S88B | $<2.2(-7)$ | 13 | 24 | 1.0(−1) | 222 | 1.8(5) | 867 | 1.12 | 8.4(4) |
| IRAS19550+3248 | $<5.1(-8)$ | 9 | 16 | 2.9(−4) | 0.35 | 1.5(2) | 6 | 0.58 | 4.1(3) |
| IRAS20188+3928 | $<1.4(-7)$ | 24 | 36 | 2.7(−3) | 1.1 | 1.3(4) | 2166 | 1.67 | 6.3(4) |
| Average: | $3.8 \pm 0.7(-8)$ | 14.3 ± 1.7 | 25 ± 2.5 | $7.0 \pm 3.2(-2)$ | 170 ± 100 | $3.5 \pm 2.2(4)$ | 690 ± 250 | 1.2 ± 0.1 | $7.0 \pm 3.4(4)$ |

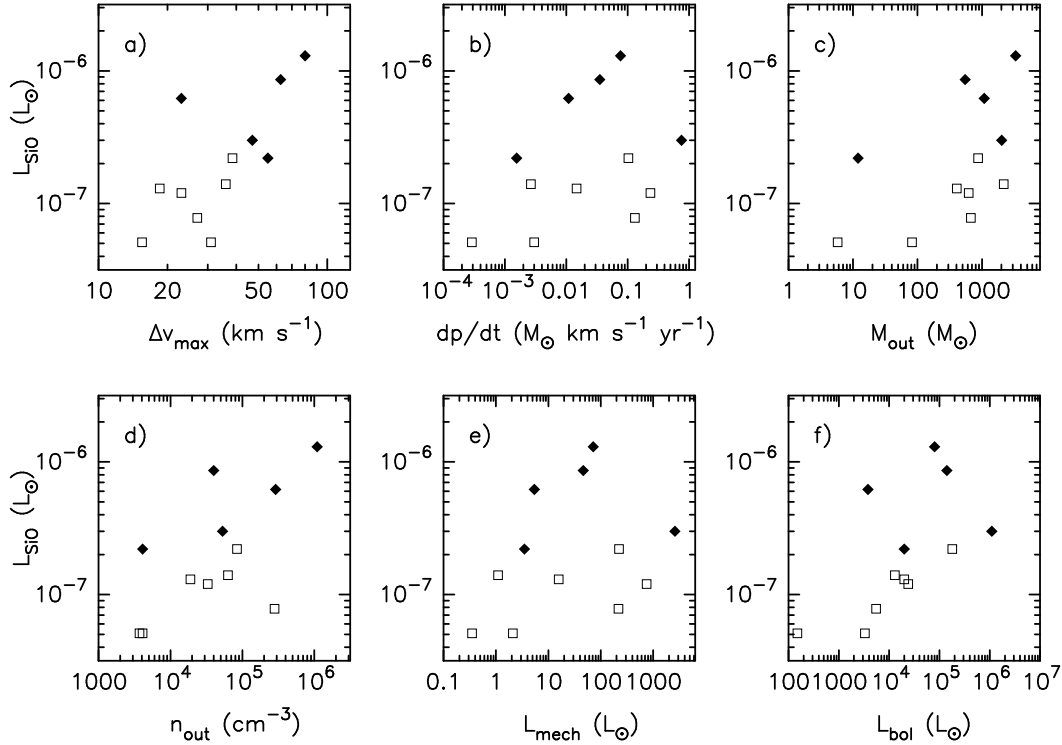


Figure 9. SiO $J=5\rightarrow 4$ luminosity as a function of various outflow parameters. Filled diamonds denote detections, open square represent $3\text{-}\sigma$ upper limits as given in Table 7.

the typical linewidth for the ambient gas (typically 8 km s^{-1} , compared with $\sim \text{few km s}^{-1}$ – e.g. Gibb et al. 2003; Fuller, Williams & Sridharan 2005). Finally, higher resolution imaging of SiO has demonstrated a clear association with the CO outflows (Hunter et al. 1999; Shepherd et al. 2004b).

Harju et al. (1998) model the emission from three bow-shock

models and conclude that the SiO is excited in a turbulent wake behind the shock front, rather than being directly associated with the shock itself. The line shapes in Figs. 1 and 2 are also consistent with this result, especially if, as is likely, the filling factor of the emission falls off with velocity (i.e. the highest velocity emission originates in the smallest volume).

5.3 Comparison with low-mass sources

To recap, 5 out of 12 sources in the current sample were detected in the 5→4 transition, a 42 per cent detection rate. This compares with a 28 per cent detection rate in the low-luminosity sources (Paper I). At first this appears to support the notion that higher-luminosity outflow sources are more likely to have detectable SiO 5→4 emission but given the small sample size (12) the detection rates are not significantly different at the 1- σ level.

The luminosity in the 5→4 line is typically 2 orders of magnitude higher for the high luminosity sources than for the low luminosity sample, though the column densities are similar between the two samples. From Paper I it is clear that none of the low luminosity sources would be detected in this survey if they were at a distance of ~ 2 kpc. Thus it is clear that the SiO emission is due to the outflows from the high-mass YSOs and not neighbouring low-mass objects.

The results of Paper I showed that SiO 5→4 emission was correlated with the outflow velocity and, to a lesser extent, the evolutionary status of the outflow driving source. As shown above (and in Fig. 9a), the outflow velocity is clearly the most significant factor in producing detectable SiO 5→4 emission.

It is harder to determine whether source age plays a similar role for massive YSOs. It is possible to examine this with a naive picture of massive star formation where the medium around a massive protostar evolves towards a lower mean density with time. Unfortunately, theories of massive star formation are still in their infancy, and there is no clearly-defined evolutionary classification for massive YSOs akin to that for low-mass YSOs. It is therefore difficult to test this hypothesis.

6 CONCLUSION

This paper has presented the results of a survey of JCMT $J=5\rightarrow 4$ SiO emission from a single-distance sample of twelve outflows from massive YSOs, mostly chosen from the Ridge & Moore (2001) CO survey. In addition, the $J=2\rightarrow 1$ transition was observed towards three of the sources detected in the 5→4 line using the BIMA interferometer.

The 5→4 transition was detected in five of the twelve sources, a detection rate of 42 per cent. This result is in good agreement with the results of a previous survey of sources covering a similar luminosity range. The detection rate is higher than that for the low mass outflow sources in Paper I, though this is not a robust conclusion at the 2- σ level.

In most cases the SiO emission is clearly associated with the outflow. NGC 6334I and AFGL 5142 show distinct red- and blue-shifted lobes in the 5→4 and 2→1 emission respectively. Simple LTE analysis yielded SiO abundances in the range of a few $\times 10^{-7}$ to 10^{-6} . However, application of an LVG model gave lower abundances ($\sim 10^{-9}$), yet predicted SiO column densities similar to those observed. The derivation of SiO abundances from the LTE analysis is therefore probably not robust. The density of the SiO-emitting regions derived from these models was typically $\sim 10^5$ cm $^{-3}$ but the temperature was not constrained over the range 50–150 K.

A comparison of the SiO 5→4 luminosity with a variety of source properties showed that the outflow velocity appears to be the primary factor which has the greatest effect on the detectability of the 5→4 transition. This result is consistent with the existence of a critical shock velocity required to disrupt dust grains and the subsequent formation of SiO in the post-shock gas. Thus SiO 5→4

appears to be a tracer of high-velocity outflows. There is also weak evidence that higher luminosity sources and denser outflows are more likely to be detected.

ACKNOWLEDGMENTS

The James Clerk Maxwell Telescope is operated by the Joint Astronomy Centre on behalf of the Particle Physics and Astronomy Research Council of the United Kingdom, the Netherlands Organization for Scientific Research and the National Research Council of Canada. The research with BIMA was funded by grant AST-0028963 from the National Science Foundation to the University of Maryland. The JCMT data were obtained as part of project M00AU19. The authors would like to thank the referee for helpful comments and Debra Shepherd for providing a copy of the CO map of G192.16–3.82.

REFERENCES

- Acord J.M., Walmsley C.M., Churchwell E., 1997, *ApJ*, 475, 693
 Anglada G., Sepulveda I., Gómez J.F., 1997, *A&AS*, 121, 255
 Birks J., Fuller G.A., Gibb A.G., 2006, *A&A*, 458, 181
 Blake G.A., Sandell G., van Dishoeck E.F., Groesbeck T.D., Mundy L.G., Aspin C., 1995, *ApJ*, 441, 689
 Bronfman L., Nyman L.-Å., May J., 2006, *A&AS*, 115, 81
 Caselli P., Hartquist T.W., Havnes O., 1997, *A&A*, 322, 296
 Codella C., Bachiller R., Reipurth B., 1999, *A&A*, 343, 585
 Davis C.J., Kumar M.S.N., Sandell G., Froebrich D., Smith M.D., Currie M.J., 2007, *MNRAS*, 374, 29
 Davis C.J., Smith M.D., Moriarty-Schieven G.H., 1998, *MNRAS*, 299, 825
 Fontani F., Caselli P., Crapsi A., Cesaroni R., Molinari S., Testi L., Brand J., 2006, *A&A*, 460, 709
 Fuller G.A., Williams S.J., Sridharan T.K., 2005, *A&A*, 442, 949
 Garay G., Köhnenkamp I., Bourke T.L., Rodríguez L.F., Lehtinen K., 1998, *ApJ*, 509, 768
 Garay G., Mardones D., Rodríguez L.F., Caselli P., Bourke T.L., 2002, *ApJ*, 567, 980
 Gibb A.G., Hoare M.G., Little L.T., Wright M.C.H., 2003, *MNRAS*, 339, 1011
 Gibb A.G., Richer J.S., Chandler C.J., Davis C.J., 2004, *ApJ*, 603, 198
 Goldreich P., Kwan J., 1974, *ApJ*, 189, 441
 Gómez Y., Rodríguez L.F., Girart J.M., Garay G., Martí, 2003, *ApJ*, 597, 414
 Harju J., Lehtinen K.K., Booth R.S., Zinchenko I., 1998, *A&AS*, 132, 211
 Hildebrand R.H., 1983, *QJRAS*, 152, 1
 Hirano N., Mikami H., Umemoto T., Yamamoto S., Taniguchi Y., 2001, *ApJ*, 547, 899
 Hunter T.R., Brogan C.L., Megeath S.T., Menten K.M., Beuther H., Thorwith S., 2006, *ApJ*, 649, 888
 Hunter T.R., Testi L., Zhang Q., Sridharan T.K., 1999, *AJ*, 118, 477
 Irvine W.M., Goldsmith P.F., Hjalmarsen Å., 1987, in Hollenbach D.J., Thronson H.A., Jr, eds, *Interstellar Processes*. Reidel, Dordrecht, p. 561
 Klein R., Posselt B., Schreyer K., Forbrich J., Henning T., 2005, *ApJS*, 161, 361
 Koo B.-C., Lee Y., Fuller G.A., Lee M.G., Kwon S.-M., Jung J.-H., 1994, *ApJ*, 429, 233
 Kumar M.S.N., Keto E., Clerkin E., 2006, *A&A*, 449, 1033
 Leurini S., Schilke P., Parise B., Wyrowski F., Güsten R., Phillip S., 2006, *A&A*, 454, L83
 Little L.T., Bergman P., Cunningham C.T., Heaton B.D., Knee L.B.G., Macdonald G.H., Richards P.J., Toriseva M., 1988, *A&A*, 205, 129
 Martín-Pintado J., Bachiller R., Fuente A., 1992, *A&A*, 254, 315
 Masson C.R., Chernin L.M., 1994, in Clemens D., Barvainis R., eds, *ASP Conf. Ser. 65, Clouds, Cores and Low Mass Stars*. Astronomical Society of the Pacific, San Francisco, p. 350

- McCutcheon W.H., Sandell G., Matthews H.E., Kuiper T.B.H., Sutton E.C., Danchi W.C., Sato T., 2000, *MNRAS*, 316, 152
Miettinen O., Harju J., Haikala L.K., Pomrén C., 2006, *A&A*, 460, 721
Mitchell G.F., Maillard J.-P., Hasegawa T.I., 1991, *ApJ*, 371, 342
Peng Y., Vogel S.N., Carlstrom J.E., 1995, *ApJ*, 455, 223
Ridge N.A., Moore T.J.T., 2001, *A&A*, 378, 495
Saito H., Saito M., Sunada K., Yonekura Y., 2007, *ApJ*, 659, 459
Schilke P., Walmsley C.M., Pineau des Forêts G., Flower D.R., 1997, *A&A*, 321, 293
Schneider N., Bontemps S., Simon R., Jakob H., Motte F., Miller M., Kramer C., Stutzki J., 2006, *A&A*, 458, 855
Shepherd D.S., 2001, *ApJ*, 546, 345
Shepherd D.S., Borders T., Claussen M., Shirley Y., Kurtz S., 2004a, *ApJ*, 614, 211
Shepherd D.S., Churchwell E., Wilner D.J., 1997, *ApJ*, 482, 355
Shepherd D.S., Kurtz S.E., 1999, *ApJ*, 523, 690
Shepherd D.S., Kurtz S.E., Testi L., 2004b, *ApJ*, 601, 952
Shepherd D.S., Watson A.M., Sargent A.I., Churchwell E., 1998, *ApJ*, 507, 861
Thompson M.A., Hatchell J., Walsh A.J., Macdonald G.H., Millar T.J., 2006, *A&A*, 453, 1003
Tieftrunk A.R., Wilson T.L., Steppe H., Gaume R.A., Johnston K.J., Claussen M.J., 1995, *A&A*, 303, 901
Turner B.E., Chan K.-W., Green S., Lubowich D.A., 1992, *ApJ*, 399, 114
Zhang Q., Hunter T.R., Sridharan T.K., Ho P.T.P., 2002, *ApJ*, 566, 982
Zhang Q., Hunter T.R., Beuther H., Sridharan T.K., Liu S.-Y., Su Y.-N., Chen H.-R., Chen Y., 2007, *ApJ*, 658, 1152
Ziurys L.M., Friberg P., 1987, *ApJ*, 314, L49
Ziurys L.M., Friberg P., Irvine W.M., 1989, *ApJ*, 343, 201

This paper has been typeset from a \TeX / \LaTeX file prepared by the author.

APPENDIX A: COVERAGE MAPS (ONLINE ONLY)

Figs A1 to A12 plot the observed grid positions relative to the CO maps for each of the sources in the survey. The CO maps are taken from RM01 except for G35.2–0.7N (Gibb et al. 2003) and G192.16–3.82 (Shepherd et al. 1998). Black dots mark the observed positions. The cross in each figure marks the location of the driving source and represents the nominal (0,0) position for the SiO mapping. The axes are arcsec offsets in RA and Dec from the (0,0) position used by RM01.

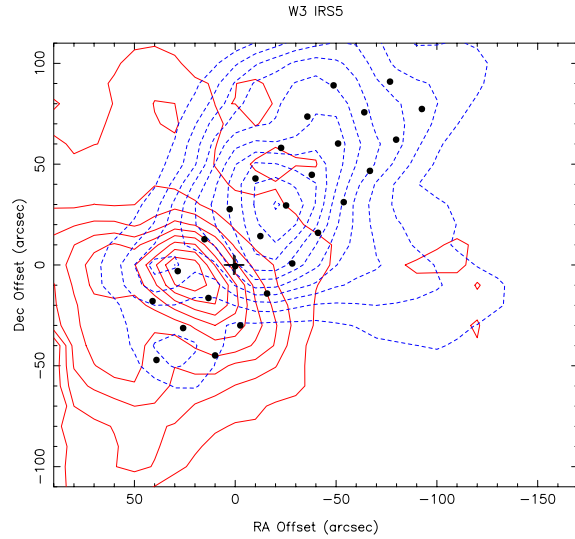


Figure A1. Coverage map for W3 IRS5.

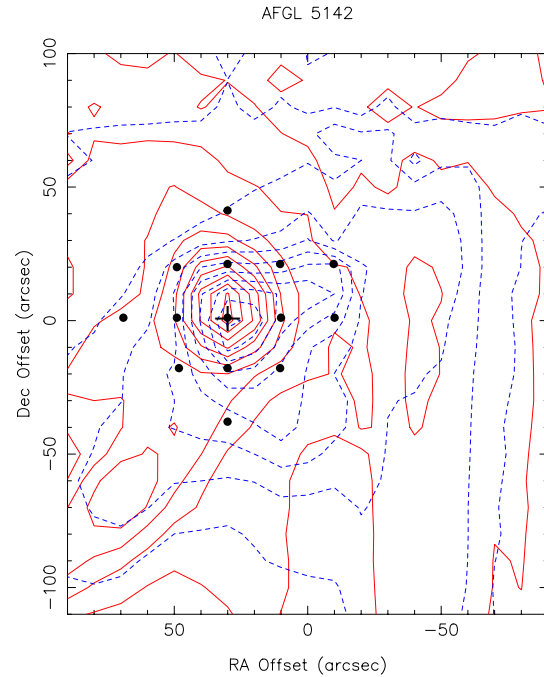


Figure A2. Coverage map for AFGL 5142.

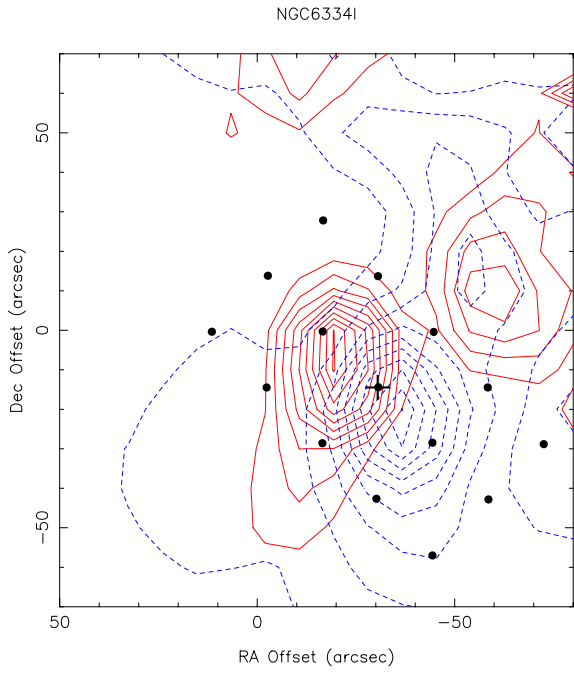


Figure A3. Coverage map for NGC 6334I.

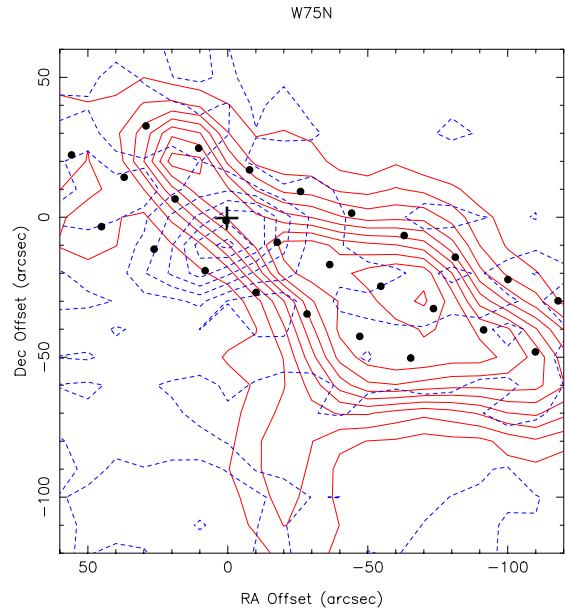


Figure A5. Coverage map for W75N.

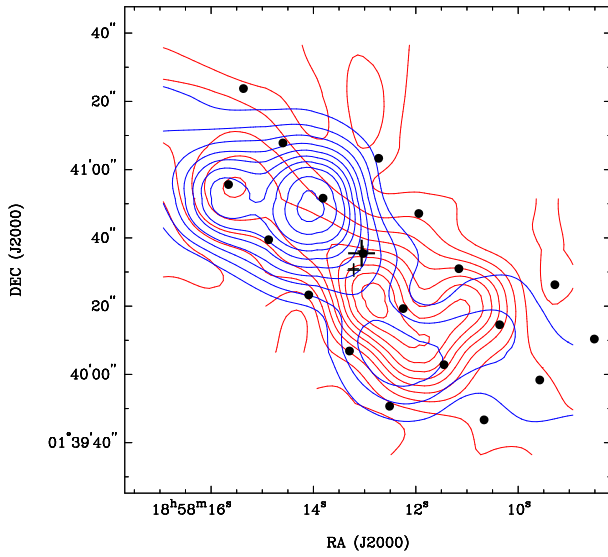


Figure A4. Coverage map for G35.2-0.7N. The smaller cross to the south-east of the large cross represents the position of MM2, the actual source for the outflow (Gibb et al. 2003; Birks et al. 2006).

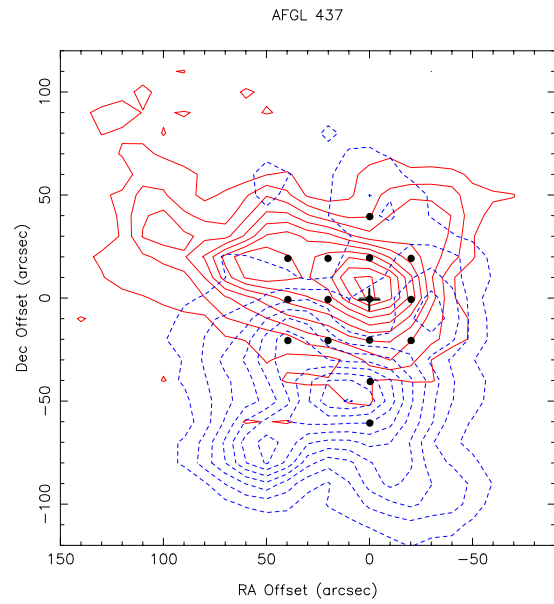


Figure A6. Coverage map for AFGL 437.

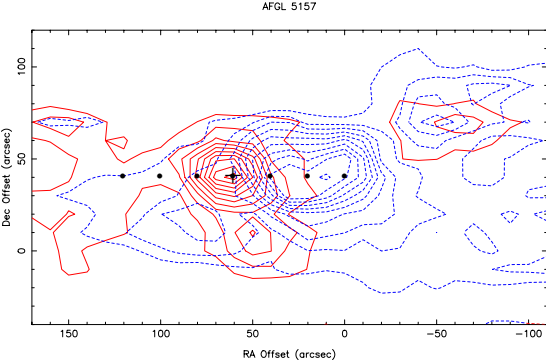


Figure A7. Coverage map for AFGL 5157.

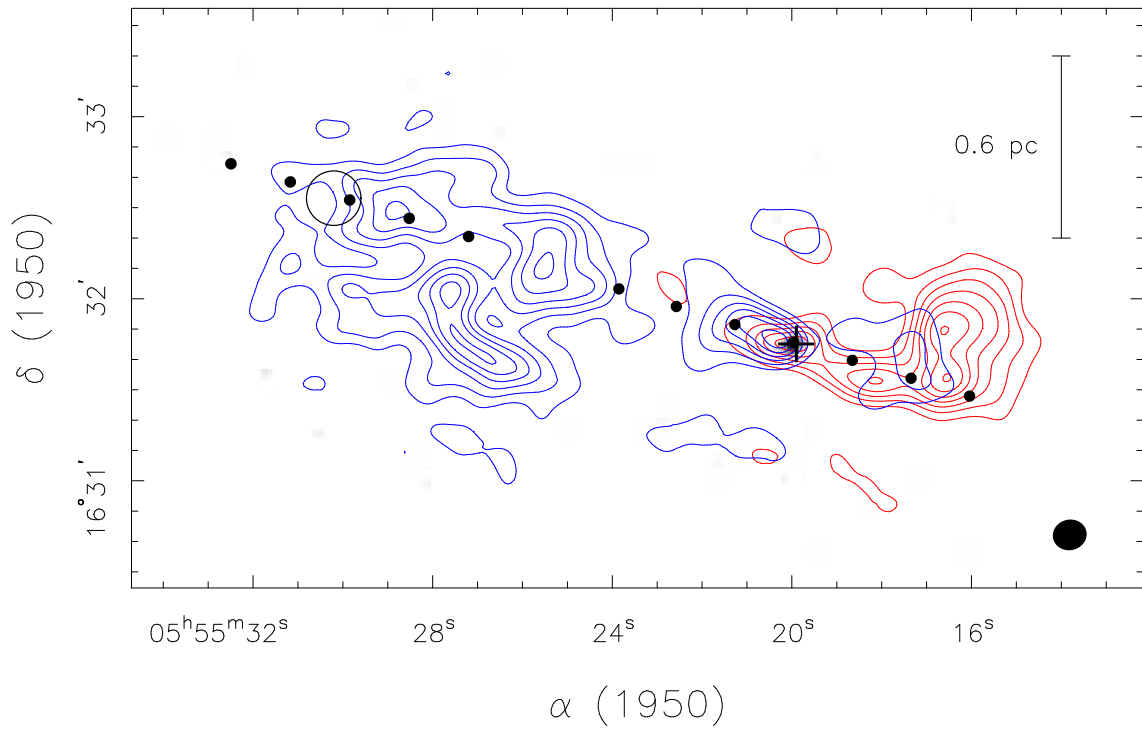


Figure A8. Coverage map for G192.16–3.82 (CO map supplied by D. Shepherd). The small open circle at the north-east of the blue lobe marks the position of the candidate HH object found by Shepherd et al. (1998).

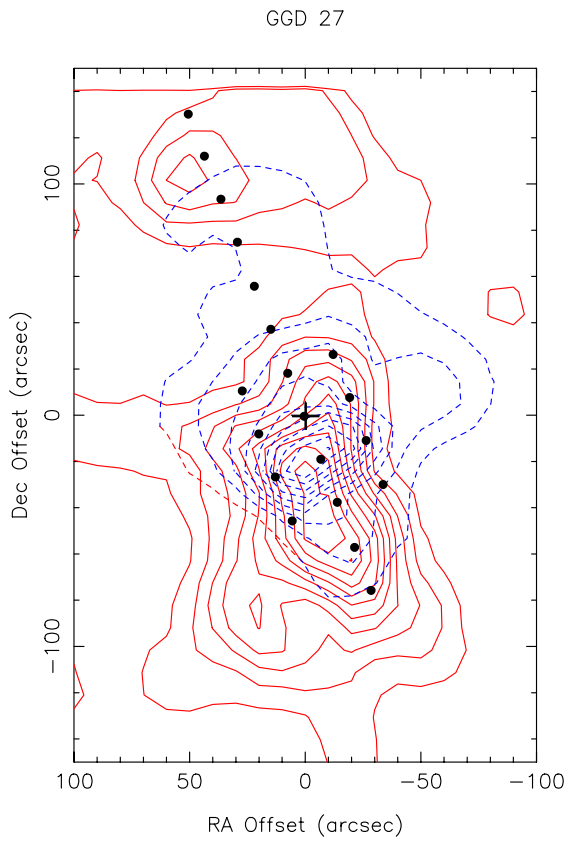


Figure A9. Coverage map for GGD27-IRS1.

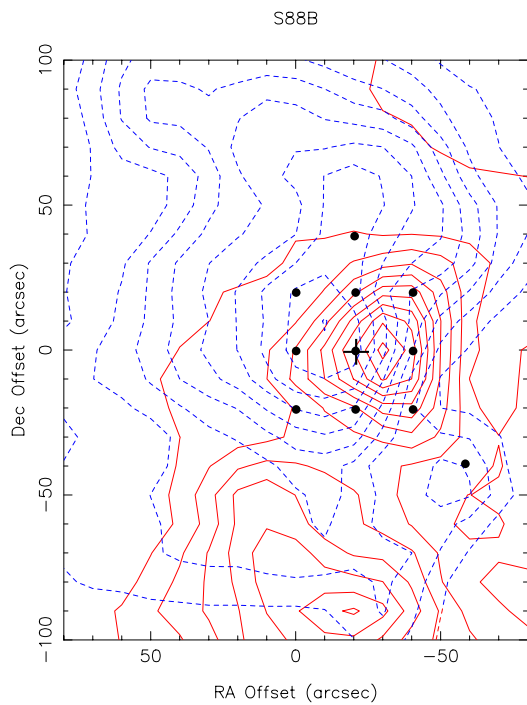


Figure A10. Coverage map for S88B.

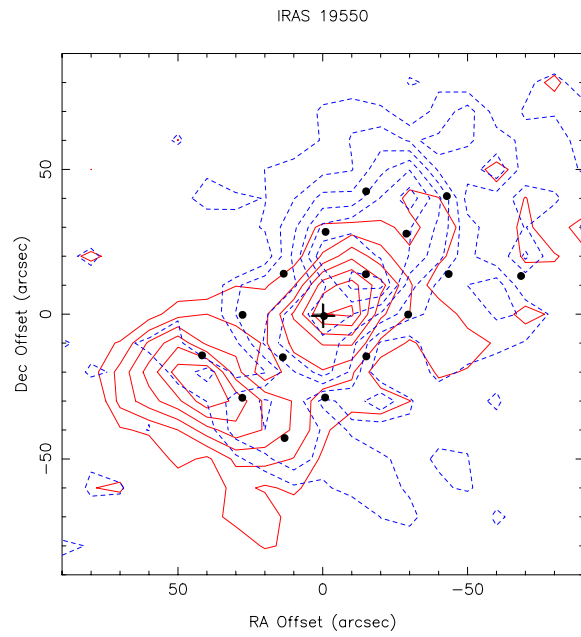


Figure A11. Coverage map for IRAS 19550+3248.

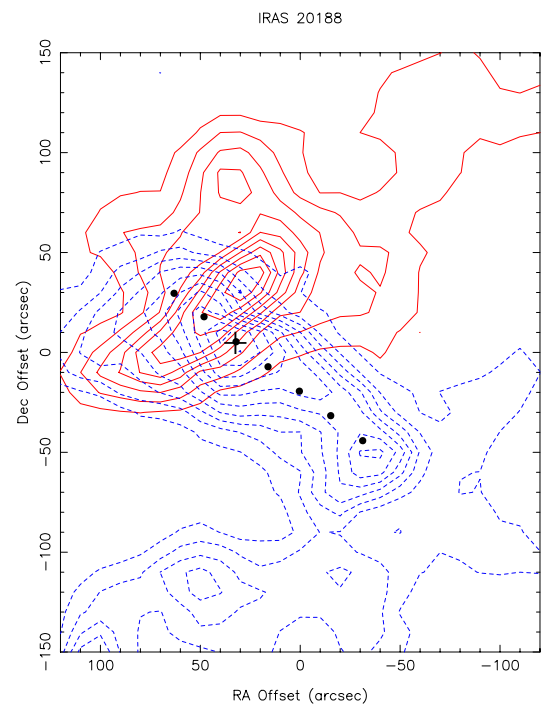


Figure A12. Coverage map for IRAS 20188+3928.